CENTRALIZED DYNAMICS AND CONTROL OF NOVEL ORBITING FORMATIONS OF TETHERED SPACECRAFT*

Marco B. Quadrelli
Jet Propulsion Laboratory, California Institute of Technology
4800 Oak Grove Drive, Pasadena, CA 91109-8099, U.S.A.
E-mail: Marco.B.Quadrelli@jpl.nasa.gov

Abstract

In this paper we investigate the interaction between an orbiting tethered system and a single spacecraft acting as leader of the tethered formation. This problem arises when a distributed sensor array formed by a chain of tethered data-gathering vehicles is being commanded to reconfigure from a remote location by the formation leader. Another example is a radar-mapping mission where multiple free-flying vehicles synthesize multiple radar apertures with the main tethered vehicle for increased coverage. In either case, a centralized control architecture distributes the information flow among the members of the sensor array. Our problem is different than conventional formation dynamics problems in that the presence of a tethered spacecraft within the formation requires an investigation of the coupling between spacecraft due to tether viscoelasticity. Examples from numerical simulation of an envisioned scenario in low Earth orbit close the paper, and demonstrate the utility of the model described to analyze similar problems. The results show that accuracy to the sub cm level or less in relative positioning and to the arc second level in relative angle can be achieved with this novel architecture.

Keywords: Formation flying, autonomous control, tethered spacecraft, distributed spacecraft.

Introduction

The objective of this paper is to develop a novel concept to coordinate clustered cooperative heterogeneous vehicles (tethered and non-tethered) in orbit. One of the main arguments for utilizing satellite formation flight for imaging applications is the fact that large sensor apertures can be synthesized without the need for correspondingly large physical structures. But other advantages to formation flight are equally compelling: these include the capability of dynamically changing the formation geometry to respond to evolving mission sensing requirements or to adapt to multiple missions.

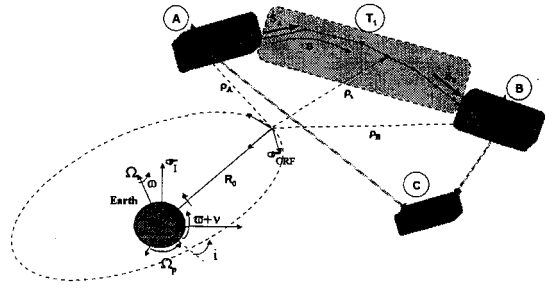

Figure 1. Model of tethered spacecraft in formation ($A+T_1+B$) with a separated leader spacecraft (C).

This can be achieved in a unique manner by combining the advantages of tethered spacecraft technology (maintaining the orbiting tethered vehicles in the same orbit at varying tether lengths without fuel cost) and formation flying technology (spatially reconfiguring the free-flying vehicles around the tethered craft on demand). Increased performance of spacecraft in planetary orbit formation can be achieved by combining (clustering) tethers deployed along the local vertical with free flier spacecraft flying in formation with the tether.

Why bother with tethering spacecraft, if formation flying is already a promising technology? Tethers, although representing a high risk/high benefit technology, have broad applications and can significantly alleviate a fuel budget for formations involving multiple cooperative vehicles. By acting as a large ultra-lightweight link between the tethered spacecraft, they enable the maintenance of very large

* Copyright © 2002 by the American Institute of Aeronautics and Astronautics, Inc. The U.S. Government has a royalty-free license to exercise all rights under the copyright claimed herein for Governmental purposes. All other rights are reserved by the copyright owner.

apertures at a fraction of the cost if the vehicles were to be maintained in close orbits by formation flying them as separated units. Being naturally gravity-gradient stabilized in virtue of their favorable moment of inertia distribution, tethered vehicles are ideal for planetary sensing. Finally, by spinning tether-connected vehicles with a very modest fuel penalty, an incredibly stable environment can be created which is virtually structurally noise free and thus ideal for optical instrumentation.

Some examples of application follow. In a formation configuration acting as a planetary sensor web, several gravity-gradient stabilized tethered vehicles in formation respond to changes in magnetic field or upper atmospheric gradients (as an array of electric dipoles immersed in a varying electric field) while a separated spacecraft tracks and maintains formation cooperation of the sensing array. This scenario would apply in orbit around any planet in the Solar System. In a formation configuration for planetary surface/subsurface imaging, a long tether (could be kilometers long) and one free-flier spacecraft fly in formation, and provide stereoscopic images of the imaged ground object. Several free-fliers operating in the same fashion would allow an increased and simultaneous coverage of the targeted area. By reconfiguring this particular formation to a different spatial topology, the different baselines between the tethered spacecraft and the free-flier units in formation can be effectively rotated in space, thus covering ground spots at different locations and of different sizes simultaneously. This scenario would also apply in orbit around any planet in the Solar System. In a formation configuration for deep space interferometry (extra-solar planet detection and imaging), two or more tethered light collectors spin around the bore sight in a very stable arrangement, and the interferometer fringes are formed at the free-flying light combiner, which, by moving around the tethered array, allows increased sky coverage. Finally, the constellation of free-flier spacecraft around the tether can act as the sensing array, while the tethered spacecraft can be considered as the information processing unit in virtue of its quasi-stationary (relative to the orbit) role enforced by gravity gradient stabilization.

This paper considers the interaction between an orbiting tethered system and a single spacecraft acting as leader of the formation (Figure 1). In Figure 1, A and B are tethered together by the link T_1, and spacecraft C is a free-flyer. Under the context of an orbiting formation definition as an ensemble of orbiting spacecraft performing a cooperative task, we point out that, until now, only spacecraft modeled as rigid bodies have been analyzed in the literature of orbiting formations and constellations. After the formation is in place, one may identify what is known as the virtual truss, i.e. the connection between the elements of the formation, which provides structural rigidity on account of the information flow between them. The virtual truss is specified by a visibility graph, which implements the connectivity in mathematical terms.

Our problem is different than conventional formation dynamics problems in that the presence of a tethered spacecraft within the formation requires an investigation of the dynamics coupling between spacecraft caused by tether viscoelasticity. Therefore, the macro-dynamics of the formation[3] due to the virtual truss is augmented by the micro-dynamics existing within the tether, namely longitudinal and lateral string dynamics. As such, this is a truly multiscale problem.

We first describe the model used for our analysis: a lumped mass approach to model tether dynamics, and models of various external perturbations acting on the system. Several vehicles are connected to and move along the tether, so that to reposition them the connecting tether links must vary in length. This feature enables distributed sensing at different spatial locations along the vertical (for a gravity-gradient stabilized tethered spacecraft). The control architecture features a separated spacecraft, which has visibility to the entire group of tethered vehicles, in the sense of the visibility graph. This vehicle is the leader of the formation, and ensures that the spacecraft on the tether remain connected and move according to a pre-specified program. The leader is also where the centralized estimator is located. This estimator continuously updates the state of the formation and estimates inter-spacecraft distance and bearing.

In this paper we present both an analytical model, as well as a numerical model, to identify some of the properties of the system under investigation. The analytical model primarily serves the purpose of identifying the major features of the interaction between a free-flying rigid spacecraft and a distributed (tethered) orbiting structure. Some of these features are: macro-modes of deformation of the virtual truss, micro-modes of deformation of the distributed structure, architecture of the formation sensor, and sources of dynamical perturbation that need to be mitigated for precision operation in space (an example being space interferometry).[1,2,3] Examples from numerical simulation of an envisioned scenario in low Earth orbit close the paper, and demonstrate the utility of the model described to analyze similar problems.

Tethered Formation Modeling

In the following we describe some features of the model currently implemented in our simulation code. The simulation is hybrid in the sense that it is part continuous (dynamics, commander, controller), part

discrete (sensing and estimation). The simulation environment possesses the following capabilities:

- Orbital/Thermoelastodynamic analysis of a system of N spacecraft connected by one or more three-dimensional tethers.
- Realistic orbital parameters representative of LEO or Heliocentric orbit. A zooming orbital reference frame approach, in which the local dynamics of the tethered system is referenced to a point, which tracks the reference orbital motion. This approach splits the dynamics in orbital with respect to inertial, and in local with respect to orbital.
- Viscoelastic tether. A critically tuned damper controls longitudinal oscillations. Tether thermal dynamics are also present. Tether dynamics represented by a finite number of lumped masses capable of large displacements. Variable tether length, commanded by varying the tether deployment and retraction rates at the end of each tether segment (assumes a point mass reel located on each spacecraft at the end of each tether).
- Non-spherical gravity field (J0 and J2 harmonics of gravitational potential). Thermal perturbations (Sun thermal/radiation input, Earth's infrared radiation, albedo). Dynamic atmospheric model (Jacchia 1977 model).
- Attitude dynamics of each spacecraft (no structural flexibility is considered) with full actuation capabilities: Proportional Thruster-Based Reaction Control System and Reaction Wheel Based Pointing Control System.
- Each spacecraft is equipped with a sensor suite composed of IRU (Inertial reference Unit with accelerometers), Gyros, Star Tracker, AFF (Autonomous Formation Flying Sensor), and tether tension and length/length rate sensor.

Formation Dynamics

We follow Figure 1. The motion of the system is described with respect to a local vertical-local horizontal (LV-LH) orbiting reference frame $(x,y,z)=F_{ORF}$ of origin O_{ORF} which rotates with mean motion Ω and orbital semi-major axis R_0. The orbital geometry at the initial time is defined in terms of its six orbital elements, and the orbital dynamics equation for point O_{ORF} is propagated forward in time under the influence of the gravitational field of the primary (Earth for LEO, Sun for Deep Space applications) and of the Earth as a third body perturbation effect. The origin of this frame coincides with the initial position of the center of mass of the system, and the coordinate axes are z along the local vertical, x toward the flight direction, and y in the orbit normal direction. The inertial reference frame $(X,Y,Z)=F_I$ is geocentric inertial for LEO (X points toward the vernal equinox, Z toward the North Pole, and Y completes the right handed reference frame), and heliocentric inertial for other applications. The orbit of the origin of F_{ORF} is defined by the six orbital elements a (semimajor axis), e (eccentricity), i (inclination), Ω_L (longitude of ascending node), ω (argument of perigee), ν (true anomaly), and time of passage through periapsis. From Figure 1, the position vector of a generic structural point with respect to O_{ORF} is denoted by $\boldsymbol{\rho}_i$, and we have $\mathbf{r}_i=\mathbf{R}_0+\boldsymbol{\rho}_i$. We define the state vector as $\mathbf{X}=(\mathbf{R}_0, \mathbf{V}_0, \boldsymbol{\rho}_1, \mathbf{q}_1, \mathbf{v}_1, \boldsymbol{\omega}_1, \ldots, \boldsymbol{\rho}_5, \mathbf{q}_5, \mathbf{v}_5, \boldsymbol{\omega}_5)^T$, where q_i and ω_i represent the quaternion and angular velocity vector of the i-th spacecraft with respect to F_I. Suppose that the spacecraft can be modeled as rigid bodies, that is, no flexible structural modes are present. Assume further that the translation dynamics and the rotational dynamics are uncoupled. The kinematics equations are as follows:

$$\begin{aligned} \mathbf{v}_i &= \dot{\rho}_i \\ \omega_i &= \Gamma(\mathbf{q}_i)\dot{\mathbf{q}}_i \\ \omega_w &= \dot{\theta}_w \end{aligned} \tag{1}$$

where $\Gamma(\mathbf{q}_i)$ is the mapping from angular velocity vector to attitude parameters, and θ_w are reaction wheel angles.

The translation dynamics equations are:

$$\ddot{\rho}_i = -\ddot{\mathbf{R}}_0 - \Omega\times\Omega\times\rho_i - 2\Omega\times\dot{\rho}_i + \frac{\mathbf{R}\ddot{\mathbf{r}}_i}{m_i} \tag{2}$$

$$\ddot{\mathbf{r}}_i = \left(\frac{\mathbf{f}_S}{m_i} - \mu_S\right)\frac{\mathbf{r}_i}{|\mathbf{r}_i|^3} - \mu_E\frac{(\mathbf{r}_i-\mathbf{r}_E)}{|\mathbf{r}_i-\mathbf{r}_E|^3} + \mathbf{A}_i\frac{\mathbf{f}_a}{m_i} \tag{3}$$

where: ρ_i = relative position vector of body i wrt. ORF, $\mathbf{A}_i$ = rotation matrix of i-th body frame wrt. inertial, $\mathbf{R}_0$ = orbital radius vector to origin of ORF, Ω = orbital rate, $\mathbf{R}$ = rotation matrix of ORF to inertial frame, f_S = magnitude of solar force, μ_S = solar gravitational parameter, μ_E = Earth gravitational parameter=3.986005×10^{14} m^3/s^2, $\mathbf{f}_a$ = actuator force, m_i = spacecraft mass with wheels added.

The rotational dynamics equations are:

$$\begin{aligned} \mathbf{J}_i\dot{\omega}_i + \dot{\mathbf{h}}_i + \omega_i\times(\mathbf{J}_i\omega_i + \mathbf{h}_i) &= \mathbf{r}_{cp2cm}\times f_S\frac{\mathbf{r}_i}{|\mathbf{r}_i|^3} + \tau_a \\ \dot{\mathbf{h}}_i &= -\tau_w \end{aligned} \tag{4}$$

where ω_i = body angular rate, $\mathbf{f}_S$ = magnitude of solar pressure, τ_a = actuator torque, τ_w = wheel input torque,

$\mathbf{J}_i$ = spacecraft moment of inertia, $\mathbf{h}_i$ = angular momentum of wheels, $\mathbf{r}_{cp2cm}$ = vector from center of mass to center of pressure of body i.

Tether Dynamics

The tether is modeled with N point masses connected by massless springs and viscous dampers. Each tether-connected spacecraft is modeled as a rigid body with internal angular momentum distribution, sensors and actuators, and mass/momentum flow representing the effect of the variable length tether.

There are two possibilities to treat tether deployment and retraction with a lumped mass model: either the mass of the mass points is kept constant (and their number will vary, implying a mass creation and elimination procedure), or the number of mass points is kept constant (and their masses will vary). The first case, in which the number of mass points varies, is more complex than the second case, and requires a state vector of varying dimension which needs to be updated during the simulation. This approach may pose significant problems when state vector variables are received from the estimator and sent to the controller. Therefore, our model assumes that the number of mass points is fixed, and the varying length kinetics is included in the equations by the correct convective terms. Our approach makes use of a material coordinate s, which describes the arc-length of the tether in the undeformed configuration. Capital I and J denote the generic end masses, while lowercase i denotes tether points. Therefore, considering the tether segment T_i, connecting masses I and J, we have that at time t, $0 \le s \le s_I(t)$ defines the tether reeled in on the I-th spacecraft, $s_J(t) \le s \le l_{total}$ defines the tether reeled in on the J-th spacecraft, and $s_I(t) \le s \le s_J(t)$ describes the deployed part of the tether. Figure 1 shows an example of this nomenclature. Clearly, $s_I(t)$ and $s_J(t)$ are prescribed functions of time representing the deployment and retrieval profiles, and we have that the currently deployed tether length is $l(t) = s_J(t) - s_I(t)$. In F_{ORF}, the position vector of a generic tether point is defined by $\boldsymbol{\rho}(s,t)$.

Let us change variables such that $s(\xi,t) = s_I(t) + \xi\, l(t)$, so that $\boldsymbol{\rho}(s,t) = \boldsymbol{\rho}(s(\xi,t),t) = \mathbf{r}(\xi,t)$. Introducing the tether nodes $\xi_i = ((i-1)/(N-1))$, $i=1,\ldots,N$, the tether element is defined by $\xi_i \le \xi \le \xi_{i+1}$. Within this element, the average position $\boldsymbol{\rho}_i(t) = (1/(\Delta\xi))\int \mathbf{r}(\xi,t)d\xi$ (where the integral is between ξ_i and ξ_{i+1}) and the mass $m_i(t) = \mu\Delta s$, where μ is the tether mass density, represent the position vector and mass of the lumped mass model. After the material differentiation operator, which introduces the convective terms depending on the current tether length and length rate, the kinematics equations of the interior tether points may be written as (i=2,...,N-1)

$$d\boldsymbol{\rho}_i/dt = \mathbf{v}_i + (1/(l\Delta\xi))\{ [(ds_I/dt)\mathbf{r}(\xi,t) + (dl/dt)\xi\mathbf{r}(\xi,t)]_{@\xi_{i+1}} - [(ds_I/dt)\mathbf{r}(\xi,t) + (dl/dt)\xi\mathbf{r}(\xi,t)]_{@\xi_{i+1}}\} \quad (5)$$

and for the I-th end body

$$d\boldsymbol{\rho}_I/dt = \mathbf{v}_I$$
$$d\mathbf{q}_I/dt = 1/2 \langle \boldsymbol{\omega}_I \rangle \mathbf{q}_I \quad (6)$$

where the <.> operator denotes a skew symmetric matrix. The dynamic equations of the interior tether point mass may be written as

$$m_i(d\mathbf{v}_i/dt) = -m_i\,\mathbf{v}_i + \mu[(ds_{i+1}/dt)(\partial\boldsymbol{\rho}(s_{i+1},t)/\partial t) - (ds_i/dt)(\partial\boldsymbol{\rho}(s_i,t)/\partial t)] - m_i\,[\mathbf{R}_0 + 2\boldsymbol{\Omega}\times\boldsymbol{\rho}_i + \boldsymbol{\Omega}\times\boldsymbol{\rho}_i\times\boldsymbol{\rho}_i] + \mathbf{f}_i^{external} + \boldsymbol{\tau}_{i+1} - \boldsymbol{\tau}_i \quad (7)$$

where $\mathbf{r}(\xi_i,t) = (\mathbf{r}_{i-1} + \mathbf{r}_i)/2$ and $(\partial\boldsymbol{\rho}(s_i,t)/\partial t) = (\mathbf{v}_{i-1} + \mathbf{v}_i)/2$. This is a finite difference approximation of the tether partial differential equation. As such, large angle tether dynamics are correctly captured, and the approximation improves with the number of tether mass points.

Finally, the tether thermal equilibrium is described by the first order differential equation

$$DT/dt = (Q^{solar} + Q^{albedo} + Q^{infrared} - 2\pi r\sigma\varepsilon T^4)/(\rho c m) \quad (8)$$

where T is the tether temperature, $Q^{[.]}$ represents an input heat flux, r is the tether radius, σ is Boltzmann's constant, ε is the tether emissivity, ρ is the tether volume density, c is the tether heat capacity, and m is the tether mass. A longitudinal damper is added in series to the tether itself at one of the tether attachment points. This is a passive damper, critically tuned to the frequency of the tether bounce mode. An additional dynamic equation represents the linear momentum balance of the tuned damper as $k_t l_t = k_d l_d + c_d(dl_d/dt)$. The total tether strain is

$$\varepsilon_{\Delta\xi} = ((l_0 + l_t + l_d + l_\theta)/l_0) - 1 \quad (9)$$

where l_0 is the tether rest length, l_t is the tether mechanical stretch, l_d is the damper mechanical stretch, and l_θ is the tether thermal stretch. The strain rate for the tether segment of length $l_{\Delta\xi}$ is

$$d\varepsilon_{\Delta\xi}/dt = [l(dl_{\Delta\xi}/dt) - l_{\Delta\xi}(dl/dt)]/l^2 \quad (10)$$

so that the tether tension in the tether segment of length $l_{\Delta\xi}$, with stiffness coefficient k and damping coefficient c, is

$$\tau_{\Delta\xi} = k\varepsilon_{\Delta\xi} + c(d\varepsilon_{\Delta\xi}/dt) \quad (11)$$

Control Model

One goal of the optimal control problem is to maintain rigidity in the formation. Another goal may be to maintain rigidity while the free-flier spacecraft is "buzzing" around the deformable system. For a system with three masses, one objective may be to let the tethered spacecraft librate about the local vertical, while the free-flier spacecraft remains a fixed distance from the tether-connected ones. Defining the current separation vectors as $\mathbf{r}_{ij}=\mathbf{r}_i-\mathbf{r}_j$ and the desired values $\mathbf{r}_{12}^d$ and $\mathbf{r}_{13}^d$, the translation error can be defined as $\mathbf{E}_{ij}=\mathbf{r}_{ij}-\mathbf{r}_{ij}^d$.

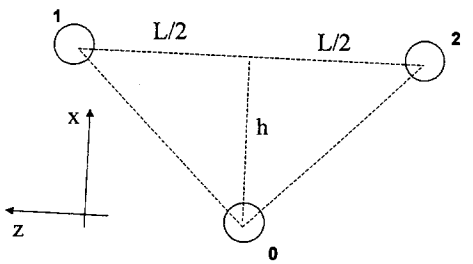

Figure 2. System geometry for control.

The objective is then to minimize the performance index

$$\hat{I}=\int_{[0,\infty)}dt\{\mathbf{E}^T\mathbf{R}\mathbf{E}+\mathbf{U}^T\mathbf{Q}\mathbf{U}\} \qquad (12)$$

subject to the dynamics of the system, where **E** is the error vector, **U** is the control vector, and **R** and **Q** denote weighting matrices.

The three-spacecraft tethered formation geometry depicted in Figure 2 requires that all spacecraft form a planar configuration. To define the planar configuration, an imaginary plane is constructed which forms the tether-attached frame. The direction cosine matrix of this tether-attached frame with respect to the inertial frame is composed of the following individual rotations $\mathbf{G}=\mathbf{R}_2(\theta)\mathbf{R}_1(\phi)F_{ORF}$, which can be derived from the tether in-plane angle θ, and the tether out-of-plane angle ϕ. For a more general deformable body than a tether (such as a beam or shell), this C-attached frame can be defined as a co-rotational frame, which in general rigidly translates and rotates with the body. The flexibility of the body itself is then defined by means of the stretch-related part of the deformation gradient, taking as a reference the rigidly rotated configuration.

As before, define the coordinates of each spacecraft by $S_i(x_i,y_i,z_i)$, where i=1,2,3. The coordinates of 1 and 2 can expressed in terms of the coordinates of spacecraft 0 by

$$\begin{aligned} &S_0:(x_0,y_0,z_0)\\ &S_1:(x_1,y_1,z_1)=(x_0+h,y_0,z_0-(l/2))\\ &S_2:(x_2,y_2,z_2)=(x_0+h,y_0,z_0-(l/2)) \end{aligned} \qquad (13)$$

The above configuration defines a virtual truss that must be maintained as rigidly as possible throughout the formation. This virtual truss can be characterized by 3 relative constraints in each axis. We define the relative error in the translation constraints by $\boldsymbol{\varepsilon}_i$, where i=0,1,2.

The problem of tethered formation flying spacecraft can now be cast as an optimal control problem. Suppose that the entire formation operates according to a leader-follower approach, where 1 and 2 are followers and 0 is the leader. A representative continuous time cost function associated with these formation constraints can be expressed by

$$Jx=\int_{[0,\infty)}dt\{\varepsilon_x^TQ_x\varepsilon_x+(d\varepsilon_x/dt)^TN_x(d\varepsilon_x/dt)+u_x^TR_xu_x\} \qquad (14)$$

(and similarly for the y and z axes, respectively) where (Q_x,Q_y,Q_z) and (N_x,N_y,N_z) are the weighting matrices associated with the error states to be defined, (u_x,u_y,u_z) are the translation forces, applied to each spacecraft that drive the error states along the three axes of motion, and (R_x,R_y,R_z) are appropriate input weighting matrices to be determined. The entries of the positive definite matrix Q_x are scaling factors that penalize error state deviations from zero to within specified requirements. Similar expressions can be given for (N_x,N_y,N_z) that penalizes the relative rate error between the neighboring spacecraft. Because of the problem symmetry and formulation simplicity, however, these matrices can be chosen to be identical and proportional to an identity matrix, that is $N_x=N_y=N_z=\kappa 1$, where $\kappa>0$. By construction, the error states describe the deviation of the constrained relative distance between each spacecraft 1 and 2 and the leader spacecraft. Therefore, the 1 and 2 must follow the leader spacecraft and maintain a pre-specified relative distance in each axis. Finally, we can also write $R_x=R_y=R_z=1$. The dynamic model for each spacecraft can be determined as derived in the first section of this paper as:

$$dX/dt=A(X)X+BU \qquad (15)$$

Further, let the desired trajectories along the three axis be denoted by x_d, y_d, and z_d. We can then write that the error vector is $E_x=[\varepsilon_x, d\varepsilon_x/dt]^T=x-x_d$. The continuous-time cost functions are equivalently expressed by (with $H=\mathrm{diag}([Q_x,N_x]))$ $J_x=\int_{[0,\infty)}dt\{E_x^THE_x+u_x^TR_xu_x\}$ subject to eq. (15) with a configuration-dependent A matrix. The continuous-time LQR optimal control laws for the x-axis of each spacecraft is given by

$$u_x=-R_x^{-1}B_xTP_xE_x \quad (16)$$

where (P_x,P_y,P_z) are the solutions to the algebraic Riccati equations

$$0=P_xA+A^TP_x-P_xBR_x^{-1}B+H \quad (17)$$

and similarly for the other axes. The existence and uniqueness of the optimal control solutions are established under the usual controllability and observability conditions. The control forces are constructed based on the relative error in the states. This means that the formulation does not require absolute knowledge of the spacecraft states; instead, it is sufficient to express the spacecraft states in terms of the formation leader's states.

Formation Commander

The translation control actually implemented on the i-th spacecraft is of the form

$$\mathbf{f}_i= \mathbf{K}_p^i(\mathbf{p}_{Cmd}^i-\mathbf{p}_{Est}^i)+ \mathbf{K}_v^i(\mathbf{v}_{Cmd}^i-\mathbf{v}_{Est}^i)+\mathbf{M}^i\mathbf{a}_{Cmd}^i \quad (18)$$

where $\mathbf{K}_p^i$ and $\mathbf{K}_v^i$ are translation control gain matrices, $\mathbf{M}^i$ is the spacecraft mass matrix, $\mathbf{p}_{Est}^i$ and $\mathbf{p}_{Cmd}^i$ represent the estimated and commanded translation state, respectively. The rotational control instead is of the following form

$$\boldsymbol{\tau}_i=\boldsymbol{\Gamma}_p^i(\boldsymbol{\lambda}(\theta_{err})_{Cmd}^i- \boldsymbol{\lambda}(\theta_{err})_{Est}^i)+ \boldsymbol{\Gamma}_p^i(\boldsymbol{\omega}_{Cmd}^i- \boldsymbol{\omega}_{Est}^i)+\mathbf{J}^i\boldsymbol{\alpha}_{Cmd}^i \quad (19)$$

where $\boldsymbol{\Gamma}_p^i$ and $\boldsymbol{\Gamma}_v^i$ are rotational control gain matrices, $\mathbf{J}^i$ is the spacecraft moment of inertia matrix, λ is the eigenaxis of rotation, θ_{err} is the magnitude of rotation corresponding to the difference between the commanded and the estimated quaternion, and $\boldsymbol{\omega}$ and $\boldsymbol{\alpha}$ are the angular velocity and acceleration respectively. The desired control forces and torques are subsequently fed to the thruster selection logic. The thruster selection logic features a nonlinear programming logic, which computes the desired on-time durations of all thrusters such that a weighted combination of force and torque errors (as differences between achievable and commanded) is minimized with the constraints of positive on-time.

Formation Estimator

A tether-attached frame (x_{te}, y_{te}, z_{te}) is defined as in Figure 3. In the example described below, it is used to specify the desired motion of the free-flyer with respect to the leader spacecrat (spacecraft 1). An estimator of the formation relative state is needed both in simulations as well as in real life because the control of the formation rigidity demands an accurate knowledge of the relative range and range rate between adjacent spacecraft. In this section we deal with the relative translation estimator only.

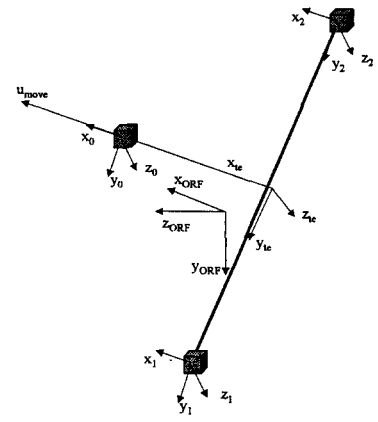

Figure 3. Depiction of tether-attached frame, orbiting frame, and spacecraft attitude frames. The unit vector labeled *umove* represents the direction of motion of the free-flier during the maneuver.

The current implementation of the translation estimator estimates only the relative position and velocity of adjacent spacecraft. This implies that the measurements used depend only on relative position and are not correlated to other system variables such as the attitude estimates of the spacecraft, or the misalignments between various subsystems. This assumption is acceptable only as long as the effects of these secondary disturbances are small compared to the errors in the relative position measurements (e.g. attitude estimate error is much less than metrology bearing measurement uncertainty). The metrology measurements are also assumed to be independent and uncorrelated between measurements, which implies that any common factor within the metrology subsystem have been removed, by calibration or estimation, in the internal processing. The radio-frequency metrology subsystem (Autonomous Formation Flying sensor) collects from each formation element receiver data of range and phase, at each of three antennae, of signals from a transmitter to three receivers on each element. This represents six one-way links for each element pair. These six links provide an RF "truss" to determine the relative position and attitude of the two elements. Assuming that all the common errors in the system have been calibrated (or solved for) and attitude is known accurately from Attitude Estimation, each link in the "truss" can be viewed as an independent measurement of the relative position of the two elements. Previous analysis has

shown that the measurement accuracy can be characterized by independent range (along the line of sight) and bearing (2 degree of freedom pointing normal to the line of sight) errors. Simulation of the AFF subsystem can be carried out on two levels, simulating individual RF links as input to an extensive processing algorithm or simulating the outputs of the process, the equivalent "truss" measurements. The latter is more suitable for a higher level system functional simulation where the subsystem low level sensor detail is not important. The perfect measurement is the vector difference of the "true" positions of the two elements of the formation, as defined by the simulation dynamics, and mapped to the coordinate system used by the Formation Estimator (if different than that used by the dynamics). The simulated output measurement vector is the perfect measurement plus an error vector randomly generated from the population represented by the measurement covariance matrix, which is also an output. Three possible information flow architectures are depicted in Figure 4.[2]

After measurement and estimation, the following input data is available to the Commander/Controller of the formation. For each spacecraft, we have: linear position, velocity, acceleration vectors, quaternion, angular velocity, angular acceleration vectors in relative bearing and bearing rate, relative range and range rate, all measured with respect to the vehicle's body frame, the neighbor spacecraft body frame, and the inertial frame. The estimation of the attitude of each spacecraft is decentralized. Star tracker and gyro measurements at each spacecraft are processed to give the spacecraft attitude relative to an inertial frame. Accelerometer and relative position measurements in the form of an AFF sensor are also available for the estimator.

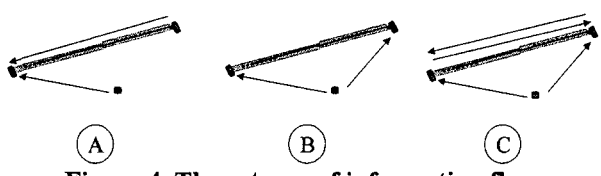

Figure 4. Three types of information flow.

The measurement covariance matrix **R** is characterized by range and bearing (2dof) estimate uncertainties and has its principal axes aligned with the measurement vector. Define the vector $\mathbf{v}=r\mathbf{u}$ where r is the range and **u** is the unit vector along the LOS, and let v_r be the variance of range estimate$=\sigma_r^2$, and v_b be the variance of bearing estimate per axis$=\sigma_b^2$. Then the measurement covariance matrix is $\mathbf{R}= v_r\mathbf{u}\mathbf{u}^T+v_b r^2(1-\mathbf{u}\mathbf{u}^T)$. A random vector from the population represented by **R** can be generated from independent, zero mean, unit variance random numbers, w_i , by $\mu_{error}=\sigma_r \mathbf{u} w_i+(\mathbf{1}-\mathbf{u}\mathbf{u}^T)$. The estimator structure is as follows:

$$
\begin{aligned}
\mathbf{r} &= \mathbf{y}-\mathbf{H}\mathbf{x} \\
\mathbf{K} &= \mathbf{X}_-\mathbf{H}^T(\mathbf{H}\mathbf{X}_-\mathbf{H}^T+\mathbf{R})^{-1} \\
\mathbf{x}_+ &= \mathbf{x}_-+\mathbf{K}\,\mathbf{r} \\
\mathbf{X}_+ &= (\mathbf{I}-\mathbf{K}\mathbf{H})\,\mathbf{X}_-\,(\mathbf{I}-\mathbf{K}\mathbf{H})^T+\mathbf{K}\mathbf{R}\mathbf{K}^T
\end{aligned}
\tag{20}
$$

where **r** is the measurement residual, **K** is the extended Kalman filter gain, **X** is the estimator state covariance, **x** the estimator state, and the subscripts + (-) denote the state before or after update. Optical metrology measurements can be treated in the same way as the RF metrology described above.

Consider the estimation of the relative position of two separated spacecraft in a geocentric orbit. Accelerometer and relative position measurements in the form of an AFF sensor are available. The relative acceleration in inertial coordinates between the center of mass of spacecraft 0 and spacecraft 1 is given by $\mathbf{a}_i=\mathbf{u}_i/m_i-\mathbf{u}_0/m_0+\mathbf{w}_i$, where m_0 and m_i are the masses of the two spacecraft and $\mathbf{u}_0$ and $\mathbf{u}_i$ are the applied forces to each of the spacecraft from sources such as thrusters, solar pressure, and gravity effects, and **w** represents kinematics terms perturbing the dynamical equation. The accelerometer measurements for one spacecraft are given in the accelerometer body frame, and their sensor model includes accelerometer bias and measurement noise. The last equation can be used to propagate the relative state measurement in the estimator.

This simplified form of the translation estimator contains only the relative (to the leader spacecraft) position and velocity vectors of the formation in an inertially fixed Reference Coordinate system. The measurements used to estimate the relative position also depend on other state variables that were assumed to be known well enough that their exclusion did not significantly change the position estimation. If those assumptions are <u>not</u> valid then those other states should be included in the estimator, significantly increasing the number of states to be estimated. Other state variables that might be included in the estimator are: Relative external/disturbance accelerations (e.g. due to solar pressure); Accelerometer bias, alignment and scale factor; Attitude of all the elements of the formation; Attitude, rate, external/disturbance angular accelerations; Gyro bias, alignment and scale factor; Location/alignment errors of all sensors within each element; Star tracker, AFF antenna array, Optical Metrology components; AFF system internal systematic errors (Relative clock offsets, Differential phase measurement biases, multipath biases); Optical Metrology internal systematic errors. Those states that can be considered constant for the duration of a set of observations (or the mission) can be solved for before

each observation (or once) in a system calibration with a separate, special purpose, estimator. These estimates of invariant states would be used as parameters in the estimator used to estimate the dynamic states during the observation period. Such calibrations usually require a series of maneuvers to make the states observable, but complete observability may still not be possible.

Formation Metrology Model

The RF metrology (AFF) subsystem collects from each formation element receiver data of range and phase, at each of 3 antennae, of signals from a transmitter on each other element. These are six one-way links for each element pair. The 6 links provide an RF "truss" to determine the relative position and attitude of the two elements. Assuming that all the common errors in the system have been calibrated (or solved for) and attitude is known accurately from Attitude Estimation, each "truss" can be viewed as an independent measurement of the relative position of the two elements. Previous analysis has shown that the measurement accuracy can be characterized by independent range errors, along the line-of-sight (LOS), and bearing errors, with two degree of freedom pointing normal to the LOS. Simulation of the AFF subsystem can be carried out on two levels, simulating individual RF links as input to an extensive processing algorithm or simulating the outputs of the process, the equivalent "truss" measurements. The latter is more suitable for a higher-level system functional simulation where the subsystem low-level detail is not important.

We call *perfect measurement* the vector difference of the "true" positions of two elements of the formation, as defined by the simulation dynamics, and mapped to the coordinate system used by the Formation Estimator. Conversely, we call *simulated output measurement* the perfect measurement plus an error vector randomly generated from the population represented by the measurement covariance matrix, which is also an output of this simulator. Previous analyses of the performance of the AFF estimate of the range and bearing between two formation elements has provided the following simplified approximations to the estimation accuracy. The assumptions of the sensor model are as follows. First, the attitude estimate accuracy is small with respect to required bearing accuracy. Second, the alignment between AFF and attitude sensors is well calibrated. Third, the AFF antenna locations with respect to s/c center of mass are well calibrated. Fourth, the AFF clock differences are well calibrated. Fifth, the AFF phase difference biases are well calibrated. AFF usually puts a large margin on this due to other noise, e.g.multipath. Observations are 6 ranges and 4 phase differences. The phase differences enhance bearing accuracy but not range. The accuracy of an estimate from one set of AFF measurements is approximately $v_{range}=v_r/6$ and $v_{bearing}=2v_{ph}/(d_i^2 + d_j^2)$ per axis, for the measurement from s/c-i to s/c-j, where d is a metric of the AFF receiver array size [meters] and may vary by element, v_r is the variance of range measurements from the ranging code correlation$\approx(1\text{cm})^2$, v_{ph} is the variance of phase measurements from carrier correlation $(10\mu\text{m})^2$.

Numerical Simulation

The parameters of the simulated prototype problem are as follows. The initial relative coordinates (in meters) of S_i, i=1, ..., 3 in the ORF are S_1(x=-250,y=0;z=0), S_2(x=0,y=0;z=-500), and S_3(x=0,y=0;z=+500). The coordinates above define a virtual formation that is to be maintained throughout the flight. The system is initially in a 800 km altitude orbit. Spacecraft masses are 100 kg. Ideal thrusters are present, with no thruster quantization effects. A set of 12 thrusters is mounted on each spacecraft, to provide full attitude and translation control authority in all directions. The tether is 960 meters long, with a 10 meter long moment arm to each connected spacecraft. Solar pressure, gravity gradient and aerodynamic drag are present in the simulation. As in [1], a longitudinal damper is placed to dissipate most of the energy on the first tether longitudinal mode.

The commander issues commands to each spacecraft as follows:

- The free-flyer spacecraft (indexed 0) is commanded to move along the moving *umove* vector from time t_1=10 seconds to time t_2=230 seconds. After that, it is required to track the attitude of the tethered spacecraft by remaining at the final distance achieved with the first maneuver.
- Spacecraft 1 is not actuated, and acts as formation leader.
- Spacecraft 2 is required to maintain the same inertial attitude as spacecraft 1.

Figure 5 shows the command profile and its time derivative adopted for the present study. The profile is a function of time of $f(t)=(3t^2T-2t^3)/T^3$ varying from 0 at $t = 0$ to a normalized value of 1 at $t = T$. The command is issued in inertial coordinates. Defining by $\mathbf{p}_{Half}$ the average inertial location of the midpoint between the two tether-connected masses, and by $\mathbf{q}_{tether}$ the attitude quaternion of the tether-attached frame, the commanded inertial position, velocity and acceleration of the free-flyer can be written as:

$$\mathbf{r}_{Cmd} = \bar{\mathbf{q}}_{I_OR} \otimes \mathbf{p}_{Half} \otimes \mathbf{q}_{I_OR} + \bar{\mathbf{q}}_{tether} \otimes (\boldsymbol{\rho}_0 + d(t)\mathbf{u}_{move}) \otimes \mathbf{q}_{tether}$$
$$\dot{\mathbf{r}}_{Cmd} = \bar{\mathbf{q}}_{I_OR} \otimes \mathbf{v}_{Half} \otimes \mathbf{q}_{I_OR} + \bar{\mathbf{q}}_{tether} \otimes (\boldsymbol{\rho}_0 + \dot{d}(t)\mathbf{u}_{move}) \otimes \mathbf{q}_{tether}$$
$$\ddot{\mathbf{r}}_{Cmd} = \bar{\mathbf{q}}_{I_OR} \otimes \mathbf{a}_{Half} \otimes \mathbf{q}_{I_OR} + \bar{\mathbf{q}}_{tether} \otimes (\boldsymbol{\rho}_0 + \ddot{d}(t)\mathbf{u}_{move}) \otimes \mathbf{q}_{tether} \tag{21}$$

where $\otimes$ denotes quaternion multiplication, the hat denotes quaternion conjugate, $\mathbf{q}_{I_OR}$ is the quaternion from ORF to inertial, ρ_0 is the initial position of the free-flyer in ORF, and d(t) is the maneuver profile as in Figure 5. The tether-attached frame has a quaternion $\mathbf{q}_{tether}$ from inertial to tether-attached frame associated with the rotation tensor

$$\mathbf{R}_{tether}=\mathbf{R}_2(\theta_{Est})\mathbf{R}_1(\phi_{E\sigma\tau})\mathbf{R}_{ORF_I}$$

$$\theta_{Est}=\text{atan2}(\mathbf{x}21(1), \mathbf{x}21(3)) \tag{22}$$

$$\phi_{E\sigma\tau}=\text{asin}(\mathbf{x}21(2)/\text{norm}(\mathbf{x}_{21}))$$

where $\mathbf{x}_{21}$ is the vector directed through the two-tether-connected masses and estimated form their current inertial location using output of the formation estimator, and i=1,2,3 denote its inertial components.

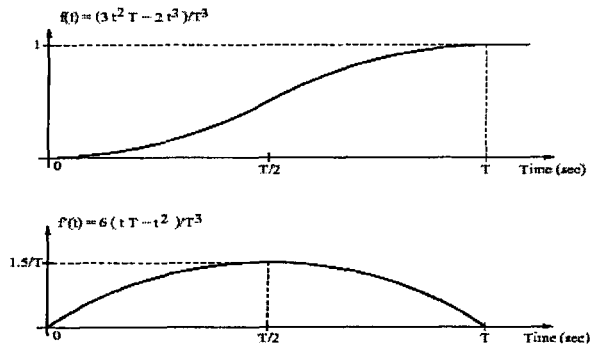

Figure 5. Depiction of commanded profile of intended repositioning of the free-flier in orbital plane.

Figure 6 depicts the overall simulation architecture, featuring the commander, controller, estimator, dynamics, and sensor and actuator models. Figures 7 and 8 show the tether temperature and the tether tension vs. time, and Figure 9 shows the tether in-plane angle rate vs. time. Figure 10 depicts the free-flyer angular error and Figure 11 the free-flyer position error during the commanded maneuver. It is evident that accuracy to the sub cm level or less in relative positioning and to the arc second level in relative angle can be achieved with this architecture and model. Figure 12 shows the attitude error of spacecraft number 2, which is required to track the attitude of spacecraft number 1 only. Figures 13 and 14 depict the tether strain and damper length respectively. Finally, Figures 15 and 16 show the force levels on two sets of thrusters during the maneuver, and Figure 17 shows the free-flyer fuel consumption vs. time.

Conclusions

In this paper we have investigated, for the first time, the dynamics, control, and estimation problem for a formation flying spacecraft composed of 3 bodies, two of which are tether-connected. This is a prototype problem, representing an example of more general hybrid tethered and non-tethered formations. Applications of such concept are envisioned in the areas of astrophysical imaging in optical wavelengths, as well as precision Earth observing imaging. The feasibility and design of a centralized command/control/estimation system to enable formation flying of spacecraft with one free flying optical module and two tethered spacecraft has been presented. The analysis includes the dynamics model in a low orbital environment, formation flying estimation, and control design with metrology and actuator models. The excellent precision performance of the system in the arc-seconds range and centimeter level during a retargeting maneuver was demonstrated by numerical simulation.

Acknowledgements

This research was carried out at the Jet Propulsion Laboratory, California Institute of Technology, under a contract with the National Aeronautic and Space Administration. The author is very grateful to Mr. Edward Mettler for useful discussions and to Dr. Fred Hadaegh for financial support.

References

[1] Quadrelli M.: *Modeling and Dynamics Analysis of Tethered Formations for Space Interferometry*, presented at the AAS/AIAA Spaceflight Mechanics Meeting, Santa Barbara, CA, February 11-14, 2001.

[4] Quadrelli M., Hadaegh, F.Y., Singh, G., and Shields, J.F.: *Some observations on the Dynamics and Control of Spacecraft Formations*, presented at the IFAC Conference on Aerospace Controls, Bologna, Italy, September 2-7, 2001.

[3] Quadrelli M.: *Effect of Distributed Rod and String Flexibility on Formation Dynamic Stability*, presented at the AAS/AIAA Spaceflight Mechanics Meeting, San Antonio, TX, January 27-31, 2002.

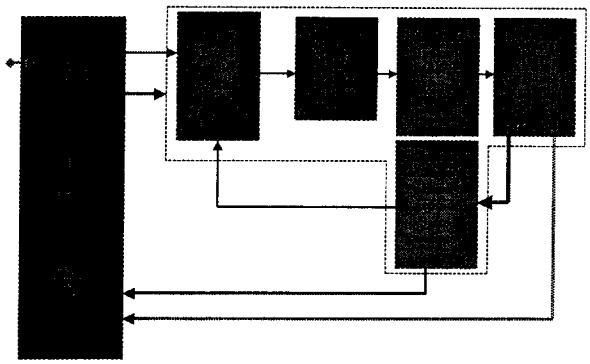

Figure 6. Simulation Architecture

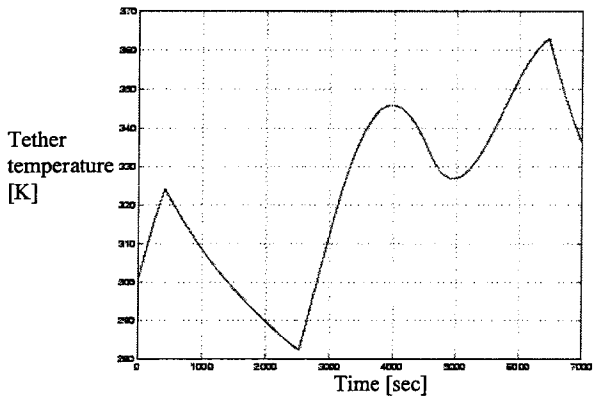

Figure 7. Tether temperature vs. time.

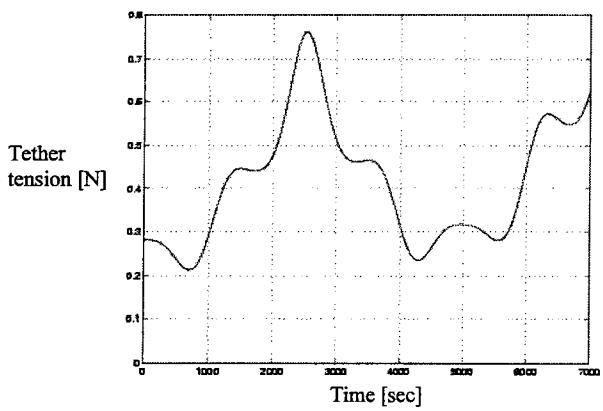

Figure 8. Tether tension vs. time.

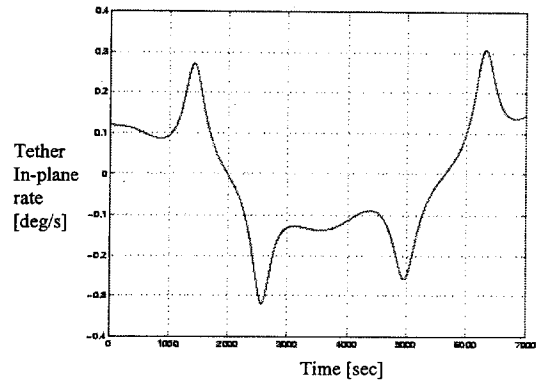

Figure 9. Tether in-plane angle vs. time.

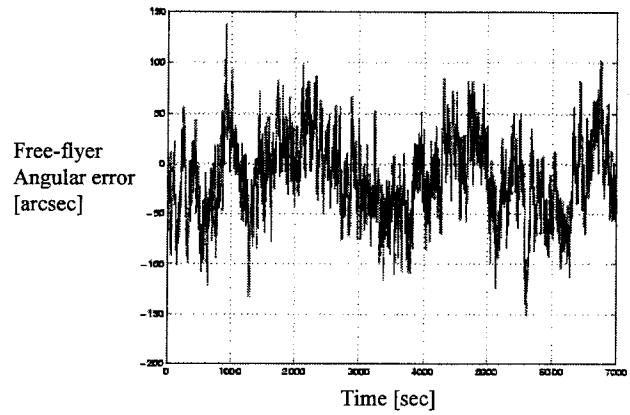

Figure 10. Free-flyer angular error vs. time.

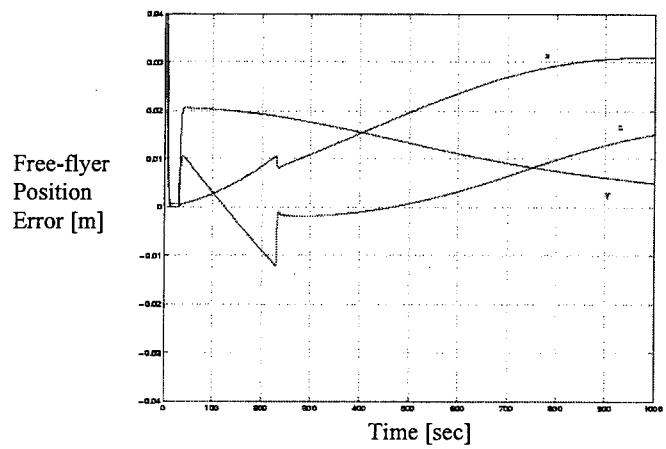

Figure 11. Free-flyer position error vs. time.

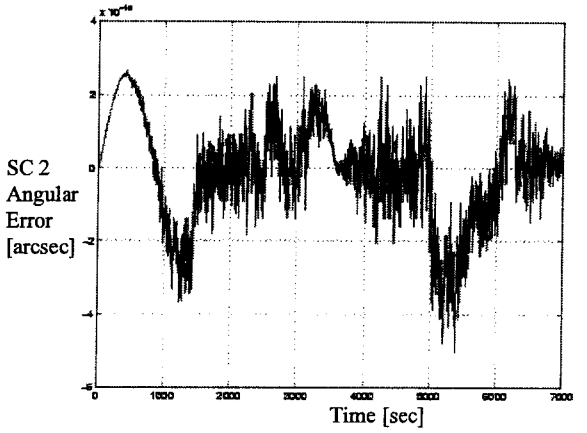

Figure 12. Spacecraft number 2 angular error vs. time.

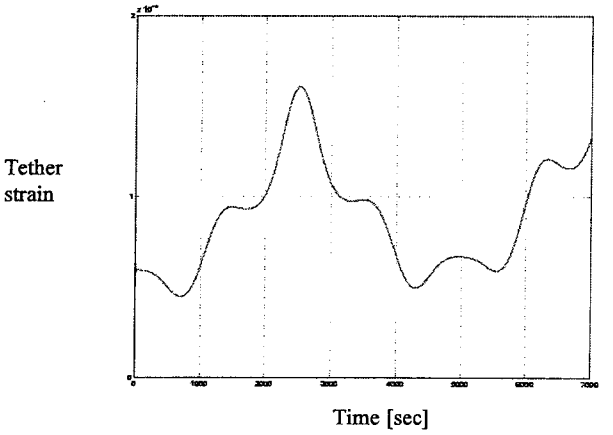

Figure 13. Tether strain vs. time.

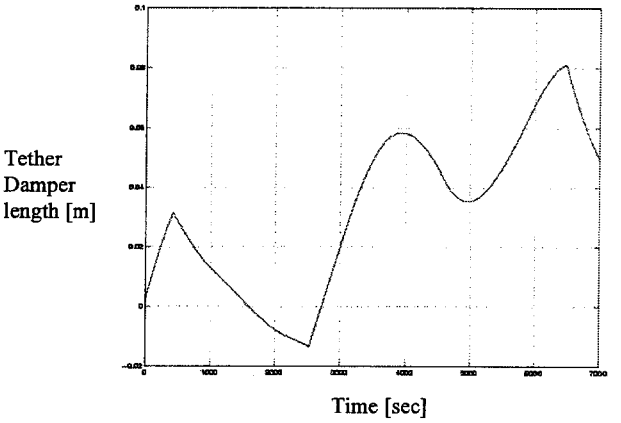

Figure 14. Tether damper length vs. time.

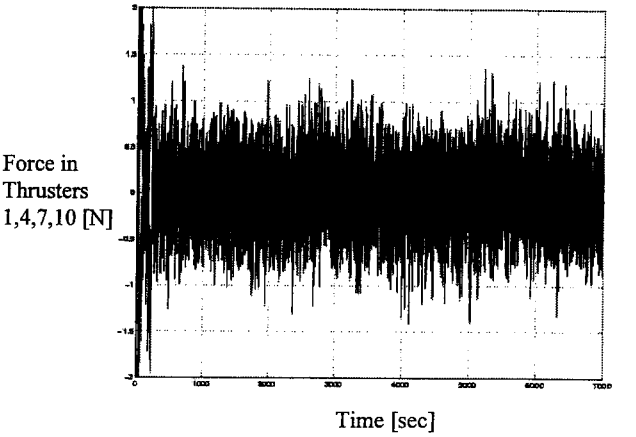

Figure 15. Force in Thrusters 1,4,7,10 vs. time.

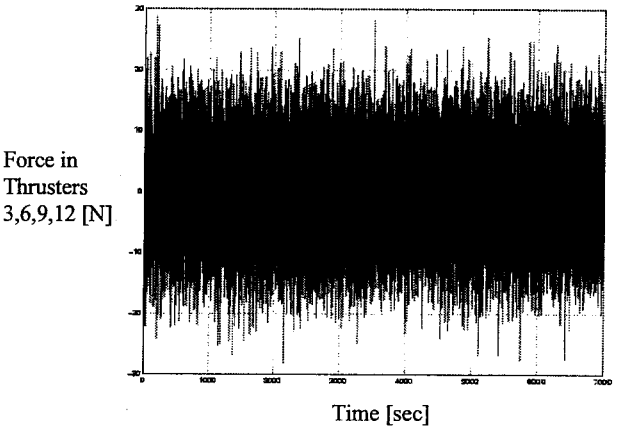

Figure 16. Force in Thrusters 3,6,9,12 vs. time.

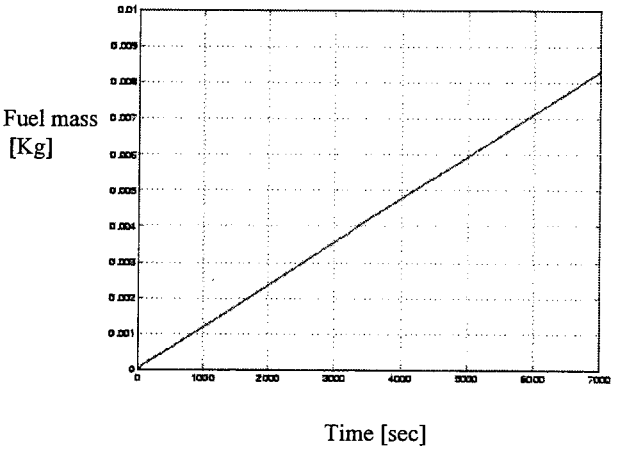

Figure 17. Free-flyer fuel consumption vs. time.